Journal of Materials Chemistry A

Accepted Manuscript

This article can be cited before page numbers have been issued, to do this please use: Y. Tian, L. Jin, H. Zhang, Z. Xu, X. Wei, E. Politova, S. Yu. Stefanovich, N. V. Tarakina, I. Abrahams and H. Yan, *J. Mater. Chem. A*, 2016, DOI: 10.1039/C6TA06353E.

ROYAL SOCIETY OF CHEMISTRY

www.rsc.org/materialsA

View Article Online
DOI: 10.1039/C6TA06353E

High energy density in silver niobate ceramics

Ye Tian,[1,2] Li Jin,[1] Hangfeng Zhang,[3] Zhuo Xu,[1] Xiaoyong Wei,[1*] E. D. Politova[4], S. Yu. Stefanovich[4,5], Nadezda V. Tarakina,[2] Isaac Abrahams,[3] Haixue Yan[2*]

[1] Electronic Materials Research Laboratory, Key Laboratory of the Ministry of Education & International Center for Dielectric Research, Xi'an Jiaotong University, Xian 710049, China
[2] School of Engineering and Materials Science, Queen Mary University of London, Mile End Road, London E1 4NS, United Kingdom
[3] School of Biological and Chemical Sciences, Queen Mary University of London, Mile End Road, London E1 4NS, United Kingdom
[4] L.Ya. Karpov Institute of Physical Chemistry, Obukha s.-st. b. 3, 105064 Moscow, Russia
[5] Lomonosov Moscow State University, Leninskie gory, 1, Moscow, 119992, Russia

***Email**: wdy@xjtu.edu.cn; h.x.yan@qmul.ac.uk

Abstract

Solid-state dielectric energy storage is the most attractive and feasible way to store and release high power energy compared to chemical batteries and electrochemical super-capacitors. However, the low energy density (*ca.*1 J cm^{-3}) of commercial dielectric capacitors has limited their development. Dielectric materials showing field induced reversible phase transitions have great potential to break the energy storage density bottleneck. In this work, dense $AgNbO_3$ ceramic samples were prepared successfully using solid state methods. Ferroelectric measurements at different temperatures reveal evidence for two kinds of polar regions. One of these is stable up to 70 °C, while the other remains stable up to 170 °C. The associated transition temperatures are supported by second harmonics generation measurements on poled samples and are correlated with the occurrence of two sharp dielectric responses. Average unit cell volume is seen to increase with increasing DC field and has been interpreted in terms of increasing levels of structural disorder in the system. At high electric field the structure becomes ferroelectric with high polarization. This field induced transition exhibits a recoverable energy density of 2.1 J cm^{-3}, which represents one of the highest known values for a lead-free bulk ceramic.

Key Words: ferroelectric, energy storage, silver niobate, phase transitions

View Article Online
DOI: 10.1039/C6TA06353E

1. Introduction

Research in the area of new energy storage technologies has been galvanized in recent years due to concerns over serious air pollution and climate change. There are growing demands for energy storage devices that have large storage ability, high efficiency, are small in size and pollution-free for applications in transportation, electronics, aerospace engineering *etc*. Among new energy storage technologies, solid-state dielectric capacitors, as used in high power electronics and related devices, have advantages in term of high power density (~ GW kg^{-1}), high charge/discharge speed (~ns) and long cycling life-time (>10^6 cycles) compared to chemical batteries and electrochemical super-capacitors.[1,2] However, the energy storage density of commercial dielectric capacitors is relatively low, (*ca.* 1 J cm^{-3} for polypropylene thin film capacitors).[3,4]

The recoverable energy density W of a dielectric material can be calculated as follows:[2]

$$W=\int_{D_{max}}^{0} E\, dD \quad (1)$$

where E is the external applied electric field and D_{max} is the electrical displacement at the highest field. Dielectric materials that exhibit a reversible phase transition from antiferroelectric (AFE) to ferroelectric (FE) behavior under high electric field represent good candidates for high energy storage devices. Lead based materials such as lead lanthanum zirconium titanate (PLZT) have been studied intensively for energy storage applications including thin film processing.[5-8] Compared to thin films, bulk ceramics have advantages in terms of cost of materials processing, and effective volume to store energy for commercial application. Moreover, environmental concerns have prompted an ongoing search for suitable lead-free replacements largely driven by legislation.[9]

Silver niobate ($AgNbO_3$) is being investigated as a possible lead-free alternative to PLZT. $AgNbO_3$ exhibits AFE-like electrical polarization under high applied electric field. Initially, $AgNbO_3$ was suggested to be ferroelectric, with an orthorhombic

View Article Online
DOI: 10.1039/C6TA06353E

perovskite structure, based on its non-linear dielectric response and X-ray powder diffraction pattern.[10,11.] Piezoelectric, pyroelectric, and electrical polarization measurements appeared to confirm the FE behavior of $AgNbO_3$[12,13]. The structure was later investigated using high-resolution X-ray powder diffraction, neutron powder diffraction, and electron diffraction by a number of research groups who found that $AgNbO_3$ shows AFE behaviour and the structure is well described by the centrosymmetric *Pbcm* space group, which is stable to around 350 °C.[14-16] However, this structure is not consistent with the occurrence of ferroelectricity, which requires the structure to be non-centrosymmetric. Fu *et al*. successfully confirmed the AFE-like nature of bulk $AgNbO_3$ through measurements of electrical polarization hysteresis loops, with the observation of double electrical polarization hysteresis under an applied field of 220 kV cm^{-1}.[17] In 2011, Yashima *et al.* suggested a non-centrosymmetric polar model in space group $Pmc2_1$ to demonstrate the structure-property relationship through a comprehensive analysis of convergent beam electron diffraction, neutron powder diffraction and synchrotron X-ray powder diffraction data.[18] They suggested that the $Pmc2_1$ structure evolves into the *Pbcm* structure when approaching 70 °C. More recently, based on calculations of defect formation energy, Moriwake *et al.* suggested polarization of randomly oriented Ag-O defect clusters in the *Pbcm* matrix, resulted in observed weak FE behavior in this system.[19]

Fabricating high quality $AgNbO_3$ bulk ceramics is challenging due to the fact that Ag_2O, typically used as a starting material, decomposes at *ca*. 200 °C,[20] which can result in large defect concentrations in the ceramics and has a significant influence on electrical properties. Here, we report the preparation of high quality $AgNbO_3$ ceramic, allowing for a detailed investigation of the structure-property relationship in this important lead free system.

2. Experimental procedure

View Article Online
DOI: 10.1039/C6TA06353E

$AgNbO_3$ ceramic samples were prepared using conventional solid-state reaction methods with sintering under flowing oxygen. Stoichiometric amounts of Ag_2O (99.7%, Sinopharm Chemical Reagent Co. Ltd, China) and Nb_2O_5 (99.99%, Sinopharm Chemical Reagent, China) powders were ball-milled in ethanol for 12 h using a planetary ball mill (QM-3SP4, Nanjing University Instrument, China). After drying, the mixtures were calcined at 850 °C for 6 h, using a pipe furnace (GLS-1600X, Hefei Kejing, China), in flowing oxygen at a rate of 500 $cm^3\ min^{-1}$. The calcined powders were milled in ethanol for 4 h and after drying, the powders were mixed with 5 wt% polyvinyl alcohol (PVA) solution and then pressed into pellets with a diameter of 1.5 cm and *ca*. 1.5 mm thickness under 400 MPa pressure. The pellets were heated at a rate of 5 °C min^{-1} to 600 °C and held at this temperature for 2 h to burn off the PVA. The samples were subsequently sintered at temperatures between 1050 and 1120 °C in oxygen at a flow rate of 500 $cm^3\ min^{-1}$ for 6 h, followed by cooling to ambient temperature at a rate 5 °C min^{-1}.

The density of the ceramic samples was measured in water using the Archimedes method. The surface morphology of the sintered samples was observed by scanning electron microscopy (SEM) (Quanta FEG 250, FEI, USA). Transmission electron microscopy (TEM) experiments were performed using a JEOL 2010 transmission electron microscope with a LaB_6 filament, operated at 200 kV. For TEM experiments, self-supported 3-mm $AgNbO_3$ discs were prepared by the following procedure: (1) samples were mechanically polished down to 300 μm, (2) 3 mm diameter discs were cut using a Gatan Ultrasonic cutter, after which they were further polished mechanically down to a thickness of 100 μm, (3) dimple grinding was performed on the two sides of each disc, using 3 μm, 1 μm and ¼ μm grits, (4) final polishing to reach electron transparency was carried out using a Gatan PIPs system, with Ar-ion beams operated at 2 kV; the beam angles were initially set to 4° and in the final stage to 2°.

For average crystalline structure analysis, the ceramic samples were crushed into fine ceramic powders. X-ray power diffraction data were collected on a PANalytical

View Article Online
DOI: 10.1039/C6TA06353E

X'Pert Pro diffractometer (PANalytical, Cambridge, UK), fitted with an X'Celerator detector, in θ/θ geometry using Ni-filtered Cu-Kα radiation (λ = 1.5418 Å), over the 2θ range 5° to 120° in steps of 0.0167°, with an effective count rate of 200 s per step. Data were calibrated with an external LaB_6 standard. For analysis of poled bulk samples, the unpolished bulk samples were first coated with silver electrodes and the samples poled with an applied field of 5 MV m^{-1} for 20 min, using a high voltage supply source. The silver electrodes were subsequently removed in acetone solution, prior to X-ray data collection. Structural analysis was carried out using the Rietveld method with the GSAS suite of programs.[21] Initial models were based on the structures reported by Levin *et al*.[16] for the non-polar structure in space group *Pbcm* and Yashima *et al*.[18] for the polar structure in space group $Pb2_1m$ (transformed from $Pmc2_1$ originally reported by Yashima *et al.*[18] to ensure axial assignments consistent with the non-polar structure).

Second harmonic generation (SHG) measurements were carried out using an optical SHG detector, with a Nd:YAG laser, λ = 1.064 μm. Measurements on poled bulk samples were carried out on heating and cooling up to *ca*. 270 °C.

Differential scanning calorimetry (DSC) was conducted on ground unpoled ceramic powder in air at a scan rate of 10 °C min^{-1}, with a Mettler Toledo DSC-822 (Mettler, Toledo, USA).

For measurement of dielectric properties, the ceramic samples were polished down to a thickness of ~0.5 mm and coated with sliver paste. The temperature-dependent dielectric permittivity on heating and cooling was obtained by measuring the capacitance with an LCR meter (an Agilent E4284) connected to a computer-controlled temperature chamber. For measurement of electrical polarization loops, the bulk samples were polished down to a thickness of ~400 μm and coated with Au electrodes. The polarization-field (*P*-*E*) and polarization current–field (*I*-*E*) loops were obtained using a ferroelectric hysteresis measurement tester (NPL, Teddington, UK). The differential permittivity- field (*dD/dE* vs. *E*) loops were calculated from the *P*-*E* loops.

View Article Online
DOI: 10.1039/C6TA06353E

3. Results and Discussion

3.1 Structure

Ceramic samples with a relative density of *ca*. 97% were obtained after sintering at 1090 °C. The resulting translucent ceramic disks were yellow in color. Scanning electron micrographs (Fig. 1) reveal block shaped grains with an average grain size of ~5 μm (Fig.1a), with the high density confirmed in images of the fracture surface (Fig. 1b).

The X-ray powder diffraction data for a ground ceramic powder of $AgNbO_3$ was modelled in both the *Pbcm* and $Pb2_1m$ space groups. A comparison of the crystal and refinement parameters is summarized in Table 1, with the fitted diffraction profiles and refined structural parameters given as supplementary data (Fig. S1 and Table S1). Both *Pbcm* and $Pb2_1m$ models fit the data well, with R_{wp} values of 0.0858 and 0.0851, respectively. An *F*-test based on extrapolation of the method of Hamilton[22] shows the improvement in the R_{wp} value in the $Pb2_1m$ model to be insignificant at the 99.5% confidence level compared to that from the *Pbcm* model. Indeed, simulated powder patterns based on the literature data for the polar and non-polar structures are virtually identical (Fig. S2). The *Pbcm* space group is a supergroup of $Pb2_1m$, but with additional systematic absences due to the *c*-glide perpendicular to the *b*-axis. There is no evidence in the X-ray diffraction data for the presence of *h*0*l* or 00*l* reflections with $l = 2n + 1$ consistent with the polar structure (Fig. 2), which suggests that the *Pbcm* space group is a better description of the average structure. Both structures are based on a $\sqrt{2}a$, $\sqrt{2}a$, $4a$ supercell of the pseudo-cubic perovskite cell, giving eight pseudo-cubic sub-cells per supercell. The structures show $(a^-,b^-,c^+)/(a^-,b^-,c^-)$ titling of the niobate octahedra.

Selected-area electron diffraction (SAED) patterns of $AgNbO_3$ (0*kl*, 0*k*0 $k = 2n$) viewed along the [-1 -1 0], [0 0 1] and [2 0 1] zone axes are shown in Figs. 3 and 4. In contrast to the X-ray experiment, there is clear evidence for the presence of 00*l* reflections with $l = 2n + 1$ (tilting experiments confirmed this was not due to double

View Article Online
DOI: 10.1039/C6TA06353E

diffraction), which breaks the systematic absence condition for a *c*-glide perpendicular to the *b*-axis (Fig.3h) and consequently the patterns can only be indexed in the lower symmetry space group $Pb2_1m$. While the SAED patterns appear to confirm polar regions, the absence of these additional reflections in the X-ray powder diffraction data indicates that the majority of the sample is non-polar.

The presence of weak 0*k*0 reflections in Fig. 3g was confirmed as being due to double diffraction. It was found that grains predominantly consist of several domains, 200-500 nm in size. Typical orientation domain boundaries are shown in Figs. 3 (c-d) and Fig. 4b. In addition to domain boundaries, numerous stacking faults along the *c*-direction of the orthorhombic lattice were observed in different grains (Figs. 3c and Fig. 4), due to the presence of additional octahedral layers in the unit cell.[23]

In order to further investigate the structural polarity of $AgNbO_3$ samples, optical second harmonics generation (SHG) measurements were carried out on heating and cooling cycles for a poled ceramic sample. The temperature dependence of the SHG signal (Fig. 5) on heating revealed a decrease in the signal up to around 170 °C, where it disappears completely. Interestingly, there appears to be a small step in the plot at around 70 °C on heating. On cooling, the SHG signal is very weak, suggesting that the majority of the sample is non-polar, which is consistent with the XRD results.

3.2 Thermal analysis and Dielectric response

The DSC thermograms on heating and cooling are shown in Fig. 6. A strong endothermic event is observed on heating at *ca.* 350 °C, with a much weaker endothermic event at *ca.* 370 °C. The corresponding exotherms on cooling occur at *ca.* 330°C and *ca.*365 °C, respectively. Using neutron diffraction, Sciau *et al.*[15] reported that silver niobate underwent a phase transition between two orthorhombic phases with different octahedral titling systems, *i.e.* $(a^-,b^-,c^+)/(a^-,b^-,c^-)$ for *Pbcm* and (a^0,b^-,c^+) for *Cmcm* space groups near 350 °C. With further increase of temperature, the orthorhombic *Cmcm* phase further evolves into a tetragonal $P4/mbm$ phase, with (a^0,b^0,c^+) titling near 380 °C. $AgNbO_3$ transforms into a cubic phase ($Pm\bar{3}m$) above

View Article Online
DOI: 10.1039/C6TA06353E

580 °C. In the present study, the thermal event at lower temperature is attributed to the *Pbcm* ↔ *Cmcm* phase transition while the weak thermal event at high temperature is assigned to the *Cmcm* ↔ *P*4/*mbm* phase transition. There are no other major thermal events below *ca*. 350 °C, which would be indicative of a first order phase transition. However, there is a significant change in slope of the baseline, which may support a second order transition at around 170 °C (Fig. 6).

Figs. 7 show the real and imaginary components of dielectric permittivity on heating and cooling cycles at 1 MHz. There is a maximum in dielectric permittivity at ca. 350 °C, which shows a degree of thermal hysteresis and is associated with the *Pbcm* ↔ *Cmcm* phase transition. A small shoulder is observed on heating at around 380 °C, consistent with the *Cmcm* ↔ *P*4/*mbm* transition. Unlike the DSC data (Fig. 6), three dielectric anomalies are observed below *ca.* 350 °C. A dielectric anomaly is clearly observed at *ca*. 70 °C (Fig. 6a), indicative of a phase transition. Furthermore, a sharp dielectric anomaly is observed near 170 °C on cooling, which is virtually undetectable on heating and has been observed previously.[24] Another broad diffuse dielectric response is seen at around 260 °C. It was suggested that in early studies that the two dielectric anomalies near 70 °C and 260 °C, were associated with two phase transitions, denoted $M_1 \leftrightarrow M_2$ and $M_2 \leftrightarrow M_3$, respectively[25,26]. There is some debate in the literature about the nature of these transitions, particularly regarding the structural details. Sciau *et al*[15] and Levin *et al.*[16] suggested that average structure of all three M phases was well described in the *Pbcm* space group. However, Yashima *et al.*[18] later reported that the $M_1 \leftrightarrow M_2$ transition involves a change in polarity (*i.e*. *Pb*2$_1$*m* to *Pbcm*). The sharp dielectric anomaly at *ca.* 170 °C is assigned to the freezing temperature (T_f) of the antipolar dipoles in the *Pbcm* lattice.[16,27] At high temperature, the antipolar dipoles are arranged randomly because Nb^{5+} cations are randomly disordered over eight sites displaced in the cubic <111> direction, although two of them are preferred.[16] On cooling the occupancy probabilities for the remaining six sites decreases gradually and vanishes below T_f, where the Nb^{5+} cations order into antipolar arrays, resulting in the sharp dielectric response observed.

View Article Online
DOI: 10.1039/C6TA06353E

3.3. Electrical polarization response and energy storage

Fig. 8 shows electric polarization loops measured at 10 Hz. A ferroelectric-like *D-E* hysteresis loop is observed below 2 MV m^{-1} (Fig. 8a). FE domain switching is confirmed by current peaks in the *I-E* loop, denoted as $\pm E_1$. The remnant polarization is about 4×10^{-4} C m^{-2} (*i.e.*, 0.04 μC cm^{-2}). This is consistent with a value reported by Kania *et al.* [12] and confirms the presence of polar regions as indicated by our TEM data. Fig. 8b depicts *D-E* and *I-E* loops under an applied field of 6 MV m^{-1}. At this higher applied field, additional broad current peaks are observed around 2.5 MV m^{-1} (denoted as $\pm E_2$). The remnant polarization is about 2.5×10^{-3} C m^{-2} (*i.e.*, 0.25 μC cm^{-2}), which is five times larger than that under an applied field of 2 MV m^{-1}. These results indicate the polarization reversal of another type of polar structure. Thus the results suggest two FE domain switching phenomena after electrical polarization.

Fig. 9 shows the thermal variation of electrical polarization at 10 Hz, with detail of the positive part of the *I-E* loops on heating and cooling, shown in Fig. 10. It can be seen that the intensity of the current peaks at $\pm E_1$ gradually decreases and the peaks disappear completely at 100 °C. Similarly, the intensity of current peaks at $\pm E_2$ also gradually decreases with increasing temperature and the peaks disappear at 180 °C. The results support the suggestion of two FE domain switching phenomena at high applied field (6 MV m^{-1}), with two different transition temperatures, which appear to correlate with the dielectric anomalies at *ca.*70 °C and 170 °C (Fig. 7).

Fig. 11 shows the variation of unit volume after poling under different DC fields. There is a clear increase in volume with increasing field. Larger unit cell volume (*i.e.* lower density) is typically the result of increased disorder, as occurs for example in order-disorder transitions. The observed increase in unit cell volume is therefore consistent with increasing structural disorder.[28] This cannot be explained by domain switching, but could be associated with a field induced transition from non-polar to polar phases at least for part of the ceramic, which results in higher remnant polarization in samples after application of an applied field (Fig.8) and is consistent with the enhanced SHG signal for poled samples (Fig.5).

View Article Online
DOI: 10.1039/C6TA06353E

Fig. 12 shows electrical polarization loops measured at 1 Hz under a maximum applied field of ±17.5 MV m^{-1}. Typical antiferroelectric-like double *P-E* behavior is observed. Field induced transitions from the initial AFE-like to FE states are marked as $\pm E_F$ (*ca.* ±12.5MV m^{-1}), while the reverse transitions are marked as $\pm E_B$. The results are consistent with those of Fu *et al.*[17] Two additional current peaks (denoted as $\pm E_U$) are observed at *ca*. 5 MV m^{-1}. The presence of the $\pm E_U$ peaks indicate that the structure exhibits remnant polarization (*ca.* 5×10^{-2} C m^{-2}) at zero field after high field cycling. The observed AFE-like double *P-E* hysteresis under high field cycling is suggested to originate from an electrical field-induced reversible intermediate polar state to an FE state. The larger remnant polarization after high field cycling compared to that after application of an intermediate field (Fig. 8), indicates that a significantly greater proportion of the sample is polar, and suggests a ferrielectric-like structure for $AgNbO_3$ after high field cycling, which is consistent with the field induced ferroelectric $Pmc2_1$ structure based on first principles calculations[29]. The field induced reversible transition to the FE state is linked with a high recoverable energy density ($W_{rec.}$ = 2.1 J cm^{-3}) in $AgNbO_3$ ceramics at room temperature. Table 2 shows the values of electrical polarization and energy density of $AgNbO_3$ compared to those of other well-known bulk ceramic materials. It can be seen that $AgNbO_3$ exhibits a higher field induced polarization and higher energy density than any other lead-free bulk ceramic.

Fig.13 shows a comparison of electrical polarization loops of a fresh sample and a sample after high field (±17.5 MV m^{-1}) cycling under a maximum field of ±6 MV m^{-1}. The measurement was carried out on cooling. The intensity of the current peaks at $\pm E_1$ showed little change between samples. In contrast, the current peaks at $\pm E_2$ show a significant increase in intensity after high-field cycling. The behavior suggests that the current peaks at $\pm E_2$ have the same origin as the $\pm E_U$ peaks (Fig.12). E_1 and E_2 decrease to zero at *ca.*70 °C and *ca.*170 °C, corresponding to the $M_1 \leftrightarrow M_2$ and T_f transitions, respectively. Both sets of current peaks shift to higher field (Fig. 14) consistent with harder domain switching at lower temperatures. The two current peaks remain down to -150 °C, indicative of two polar structures.

View Article Online
DOI: 10.1039/C6TA06353E

4. Conclusions

Single phase $AgNbO_3$ ceramics were successfully prepared, with relative densities above 97%. While X-ray powder diffraction is unable to distinguish between polar and non-polar structures, TEM results suggest the presence of submicron polar regions. This is consistent with observed domain switching in ferroelectric loops at low fields up to 70 °C. At fields of around ±6 MV m^{-1} a further ferroelectric domain switching phenomenon occurs and is attributed to a field induced transition (non-polar to polar) up to 170 °C (T_f), confirming the structure is polarizable below this temperature. At a much higher field of ±17.5 MV m^{-1}, there is a transition from a ferrielectric-like structure to a ferroelectric structure, the latter exhibiting a high polarization (40 μC cm^{-2}). This transition is associated with a recoverable energy density of 2.1 J cm^{-3}, which is one of the highest known values for a bulk dielectric ceramic and double the value of materials currently used in commercial devices for dielectric energy storage.

Acknowledgement

This work was supported by the National Basic Research Program of China (973 Program) under Grant No. 2015CB654602, the International Science & Technology Cooperation Program of China (Grant No. 2013DFR50470), the Natural Science Basis Research Plan in Shaanxi Province of China (Grant No. 2015JM5199), the Fundamental Research Funds for the Central Universities, and "111" Project (No. B14040). Especially, Ye Tian acknowledges the financial support from the China Scholarship Council.

References

1. Q. Li, L. Chen, M. R. Gadinski, S. Zhang, G. Zhang, H. Li, A. Haque, L. Q. Chen, T. Jackson and Q. Wang, *Nature*, 2015, **523**, 576.

View Article Online
DOI: 10.1039/C6TA06353E

2. Z. Dang, J. Yuan, S. Yao and R. Liao, *Adv. Mater.*, 2013, **25**, 6334.
3. M. Rabuffi and G. Picci, *IEEE T. Plasma. Sci.*, 2002, **30**, 1939.
4. X. Wei, H. Yan, T. Wang, Q.Hu, G. Viola, S. Grasso, Q. Jiang, L. Jin, Z. Xu, and M. J. Reece, *J. Appl. Phys.*, 2013, **113**, 024103.
5. G. R. Love, *J. Am. Ceram. Soc.*, 1990, **73**, 323.
6. X. Hao, J. Zhai, L. B. Kong and Z. Xu, *Prog. Mater. Sci.*, 2014, **63**, 1.
7. Y. Zhao, X. Hao and Q. Zhang, *ACS Appl. Mater. Interfaces*, 2014, **6**, 11633.
8. M. S. Mirshekarloo, K. Yao and T. Sritharan, *Appl. Phys. Lett.*, 2010, **97**, 142902.
9. R. Nevin, *Environ. Res., Sect. A*, 2000, **83**, 1.
10. M. H. Francombe and B. Lewis, *Acta Cryst.*, 1958, **11**, 175.
11. A. Reisman and F. Holtzberg, *J. Am. Chem. Soc.,*1958*,* **80**, 6503.
12. A. Kania, K. Roleder and M. Lukaszewski, *Ferroelectrics*, 1984, **52**, 265.
13. A. Kania and K. Roleder, *Ferro. Lett. Sec.*, 1984, **2:2**, 51.
14. J. Fábry, Z. Zikmund, A. Kania and V. Petrícek, *Acta Cryst.*, 2000*,* **C56**, 916.
15. P. Sciau, A. Kania, B. Dkhil, E. Suard and A. Ratuszna, *J. Phys.: Condens. Matter,* 2004**, 16,** 2795.
16. I. Levin, V. Krayzman, J. C. Woicik, J. Karapetrova, T. Proffen, M. G. Tucker and I. M. Reaney, *Phys.Rev.B,*2009, **79**, 104113.
17. D. Fu, M. Endo, H. Taniguchi, T. Taniyama and M. Itoh, *Appl. Phys. Lett.,* 2007, **90**, 252907.
18. M. Yashima, S. Matsuyama, R. Sano, M. Itoh, K. Tsuda and D. Fu, *Chem. Mater.*2011, 23, 1643.
19. H. Moriwake, C. A. Fisher, A. Kuwabara and D. Fu, *Jpn. J. Appl. Phys.,* 2013, **52**, 09KF08.
20. M. Valant, A. Axelsson and N. Alford, *J. Euro. Ceram. Soc.*, 2007*,* **27**, 2549.
21. A. C. Larson, R. B. Von Dreele, *Los Alamos National Laboratory Report*, 1987, No. LAUR-86-748.
22. W. C. Hamilton, *Acta Crystallogr.*, 1965, **18**, 502.
23. M. Verwerft , G. V. Tendeloo, J. V. Landuyt and S. Amelinckx,

View Article Online
DOI: 10.1039/C6TA06353E

Ferroelectrics,1989, **97**, 5.

24. A. Kania and J. Kwapulinski, *J. Phys.: Condens. Matter,* 1999*,* **11**, 8933.
25. J. Petzelt, S. Kamba, E. Buixaderas, V. Bovtun, Z. Zikmund, A. Kania, V. Koukal, J. Pokorny, J. Polivka, V. Pashkov, G. Komandin and A. Volkov, *Ferroelectrics* 1999, **223**, 235.
26. M. Pawelczyk, *Phase Transit.* 1987, **8,** 273.
27. S. Miga, A. Kania and J. Dec, *J. Phys.: Condens. Matter*, 2011, **23**, 155901.
28. "Handbook of Materials Modelling, Part A: Methods", Ed. S. Yip, Springer, Dorecht, The Netherlands 2005, p2045.
29. H. Moriwake, A. Konishi, T. Ogawa, C. A. J. Fisher, A. Kuwabara and D. Fu, *J. Appl. Phys.* 2016, **119**, 064102.
30. J. Wang, T. Yang, S. Chen and G. Li, *Mater. Res. Bull.*, 2013, **48**, 3847.
31. Z. Liu, X. Chen, W. Peng, C. Xu, X. Dong, F. Cao and G. Wang, *Appl. Phys. Lett.*, 2015,**106**, 262901.
32. F. Gao, X. Dong, C. Mao, W. Liu, H. Zhang, L. Yang, F. Cao and G. Wang, *J. Am. Ceram. Soc.*, 2011, **94**, 4382.
33. H. Borkar, V. N. Singh, B. P. Singh, M. Tomar, V. Gupta and A. Kumar, *RSC Adv.*, 2014, **4**, 22840.
34. L. Luo, B. Wang, X. Jiang and W. Li, *J. Mater. Sci.,* 2014, **49**, 1659.
35. Q. Xu, T. Lia, H. Hao, S. Zhang, Z. Wang, M. Cao, Z. Yao and H. Liu, *J. Eur. Ceram. Soc.*, 2014, **34**, 1209.
36. L. Wu, X. Wang and L. Li, *RSC Adv.*, 2016, **6**, 14273.
37. Z. Shen, X. Wang, B. Luo and L. Li, *J. Mater. Chem. A*, 2015, **3**, 18146.
38. T. Wang, L. Jin, C. Li, Q.Hu and X. Wei, *J. Am. Ceram. Soc.,* 2015, 98, 559.
39. Q. Hu, L. Jin, T. Wang, C. Li, Z. Xing, X. Wei, *J. Alloys and Compds*., 2015, **640**, 416.
40. V. S. Puli, D. K. Pradhan, D. B. Chrisey, M. Tomozawa, G. L. Sharma, J. F. Scott and R. S. Katiyar, *J. Mater. Sci.,* 2013, **48**, 2151.
41. B. Qu, H. Du and Z. Yang, *J. Mater. Chem. C*, 2016, **4**, 1795.

View Article Online
DOI: 10.1039/C6TA06353E

42. Z. Song, H. Liu, S. Zhang, Z. Wang, Y. Shi, H. Hao, M. Cao, Z. Yao, Z. Yu, *J. Euro. Ceram. Soc.*, 2014, **34**, 1209.

View Article Online
DOI: 10.1039/C6TA06353E

Table 1 Comparison of crystal and refinement parameters for $AgNbO_3$ ground ceramic powder at 20 °C in polar and non-polar space groups. Estimated standard deviations are given in parentheses.

Chemical formula	$AgNbO_3$	$AgNbO_3$
Formula weight	248.77	248.77
Crystal system	Orthorhombic	Orthorhombic
Space group	*Pbcm*	$Pb2_1m$
Unit cell dimensions	a = 5.5509(1) Å	a = 5.5510(1) Å
	b = 5.6060(1) Å	b = 5.6062(1) Å
	c = 15.6552(4) Å	c = 15.6558(4) Å
Volume	487.16(3) Å^3	487.21(3) Å^3
Z	8	8
Density (calculated)	6.784 g cm^{-3}	6.783 g cm^{-3}
R-factors[a]	R_{wp} = 0.0858	R_{wp} = 0.0851
	R_p = 0.0637	R_p = 0.0633
	R_{ex} = 0.0607	R_{ex} = 0.0607
	R_F2 = 0.0703	R_F2 = 0.0705
Total no. of variables	42	55
No of profile points used	6580	6580

[a] For definition of R-factors see reference [21]

Table 2 Comparison of energy storage capability of bulk ceramics

Dielectrics	Ceramic compositions	W_{rec} (J cm^{-3})	D_m (μC cm^{-2})	E_m (kVcm^{-1})	Ref.
AFE-like	$(Pb_{0.85}Ba_{0.08}Sr_{0.03}La_{0.03})(Zr_{0.74}Sn_{0.22}Ti_{0.04})O_3$	1.24	~20	100	Wang[30]
	$(Pb_{0.97}La_{0.02})(Zr_{0.58}Sn_{0.335}Ti_{0.085})O_3$	1.37	~25	86	Liu[31]
	$0.89(Na_{0.5}Bi_{0.5})TiO_3$-$0.06BaTiO_3$-$0.05(K_{0.5}Na_{0.5})NbO_3$	0.59	29.8	56	Gao[32]
	$(Na_{0.42}Bi_{0.44}Al_{0.06}Ba_{0.08})TiO_3$	0.4-0.6	~20	50	Borkar[33]
	$0.90(Na_{0.5}Bi_{0.5})TiO_3$-$0.10KNbO_3$	1.17	~30	104	Luo[34]
	$0.9[(0.92Na_{0.5}Bi_{0.5})TiO_3$-$0.08BaTiO_3]$-$0.1NaNbO_3$	0.71	28.8	70	Xu[35]
	$AgNbO_3$	**2.1**	**40**	**175**	**This work**
Relaxor-FE	$0.91BaTiO_3$-$0.09BiYbO_3$	0.71	~15	93	Shen[36]
	$0.85BaTiO_3$-$0.15Bi(Zn_{2/3}Nb_{1/3})O_3$	0.79	–	131	Wu[37]
	$0.85BaTiO_3$-$0.15Bi(Mg_{2/3}Nb_{1/3})O_3$	1.13	~25	140	Wang[38]
	$0.88BaTiO_3$-$0.12Bi(Mg_{1/2}Ti_{1/2})O_3$	1.81	~20	220	Hu[39]
	$Ba(Zr_{0.2}Ti_{0.8})O_3$-$(Ba_{0.85}Ca_{0.15})TiO_3$.	0.68	36	70	Puli[40]
	$0.80(K_{0.5}Na_{0.5})NbO_3$-$0.20Sr(Sc_{0.5}Nb_{0.5})O_3$	2.02	~15	293	Qu[41]
Paraelectrics	$(Ba_{0.4}Sr_{0.6})TiO_3(Ba_{0.4}Sr_{0.6})TiO_3$	1.28	~20	243	Song[42]

View Article Online
DOI: 10.1039/C6TA06353E

Figures

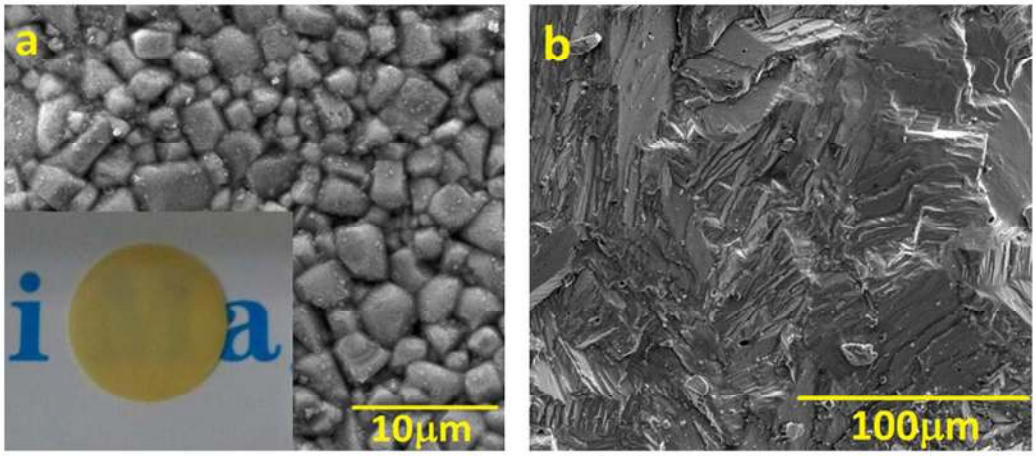

Fig.1. Scanning Electron Micrographs of $AgNbO_3$ ceramic, (a) original surface with an image the ceramic disk inset and (b) fracture surface.

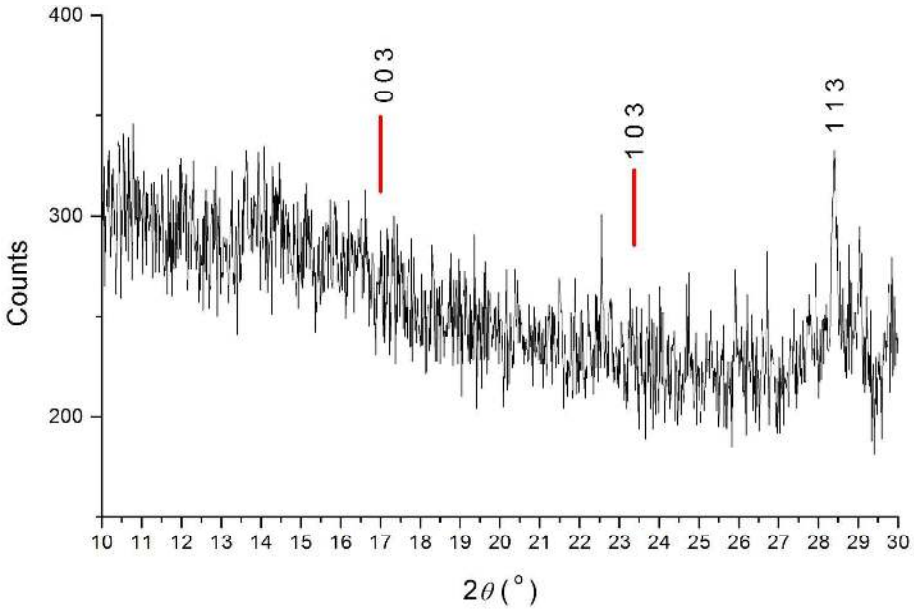

Fig. 2. Detail of the X-ray diffraction pattern for $AgNbO_3$ ground ceramic powder, showing positions of absent (003) and (103) reflections compared to the observed (113) reflection.

View Article Online
DOI: 10.1039/C6TA06353E

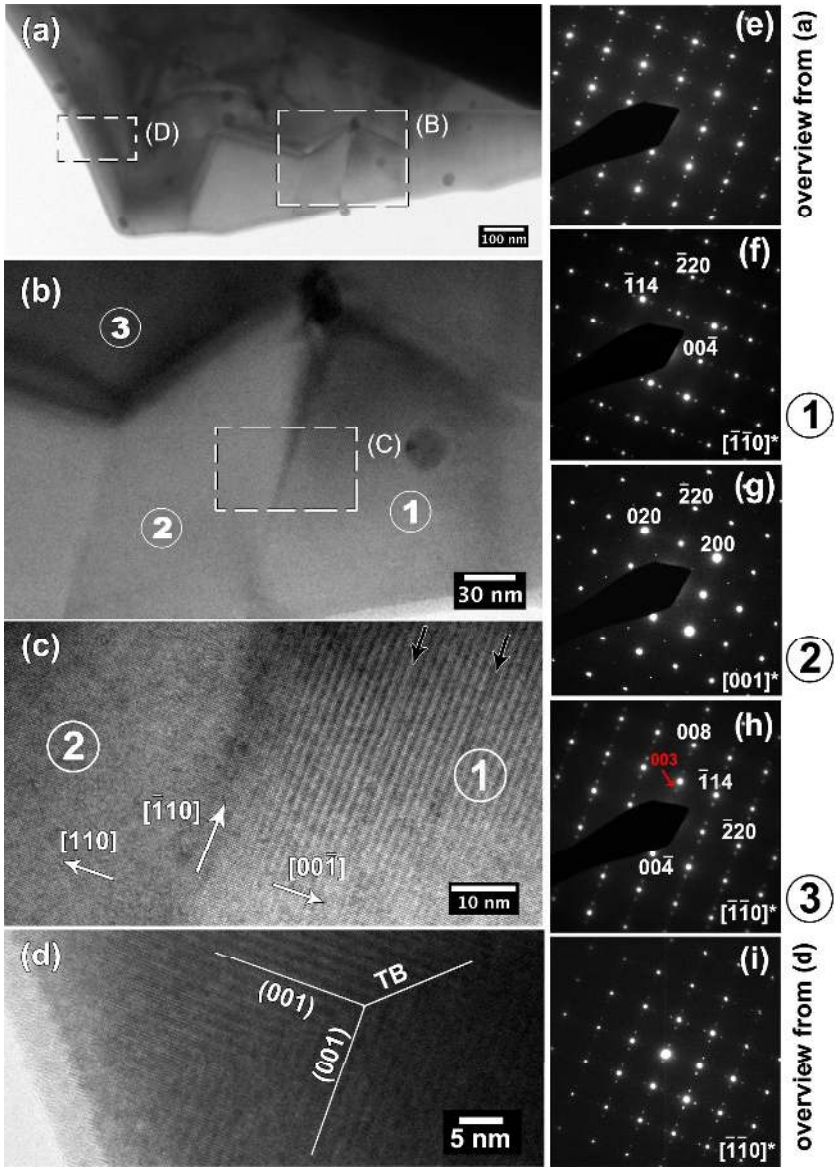

Fig. 3. (a) Overview bright-field image of a grain with several domains; (b) enlargement of the area labeled (B) in (a); (c) high-resolution transmission electron microscopy image of the interface between domains labeled (1) and (2), black arrows indicate the positions of stacking faults; (d) high-resolution transmission electron microscopy image of the area labeled (D) in (a) exhibiting a twin boundary; (e) SAED pattern resulting from the overlapping of diffraction patterns from domains shown in (a); (f), (g), (h) SAED patterns taken from the domains labeled (1), (2) and (3), respectively. (i) SAED patterns taken from the area shown in (D). SAED patterns are indexed in the $Pb2_1m$ space group. 'TB' stands for a twin boundary. The red arrow in (h) indicates the 003 reflection.

View Article Online
DOI: 10.1039/C6TA06353E

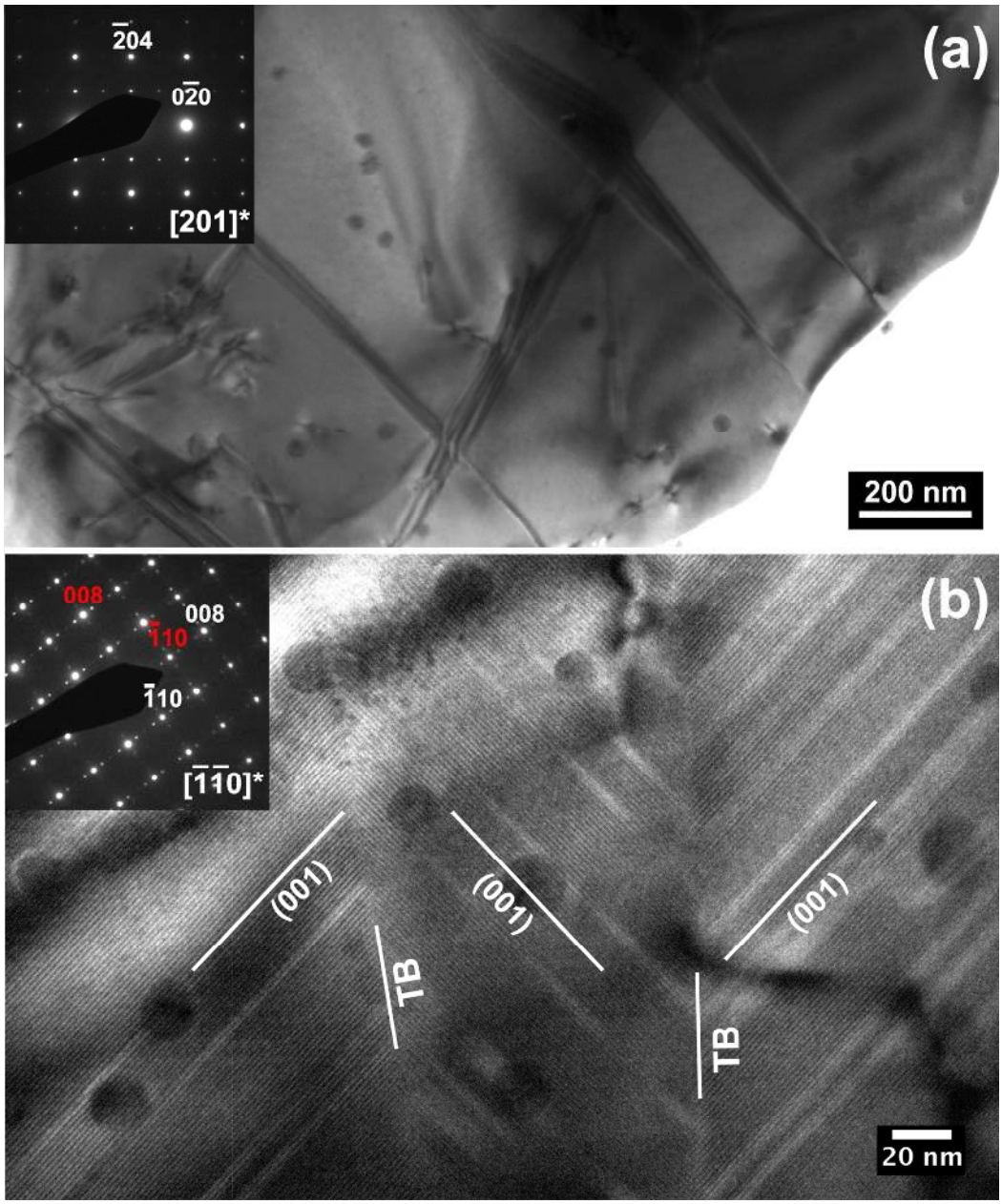

Fig. 4. (a) Bright-field image of $AgNbO_3$ showing several fringe patterns due to stacking faults. (b) Diffraction contrast image of twin domains in $AgNbO_3$ displaying many stacking faults. 'TB' denotes a twin boundary. Inset: SAED patterns indexed in the $Pb2_1m$ space group.

View Article Online
DOI: 10.1039/C6TA06353E

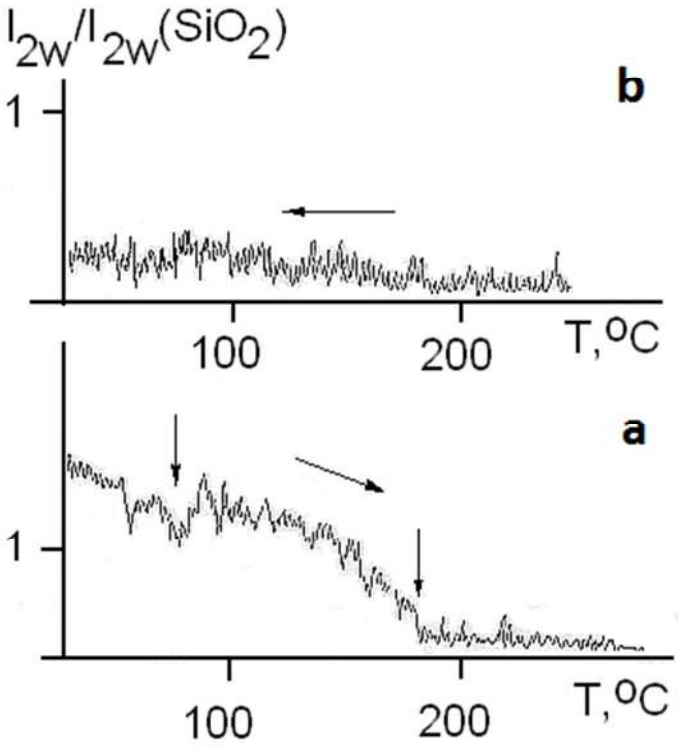

Fig. 5. Temperature dependence of the SHG signal $q = I_{2w}/I_{2w}(SiO_2)$ on (a) heating and (b) cooling of a poled ceramic sample.

View Article Online
DOI: 10.1039/C6TA06353E

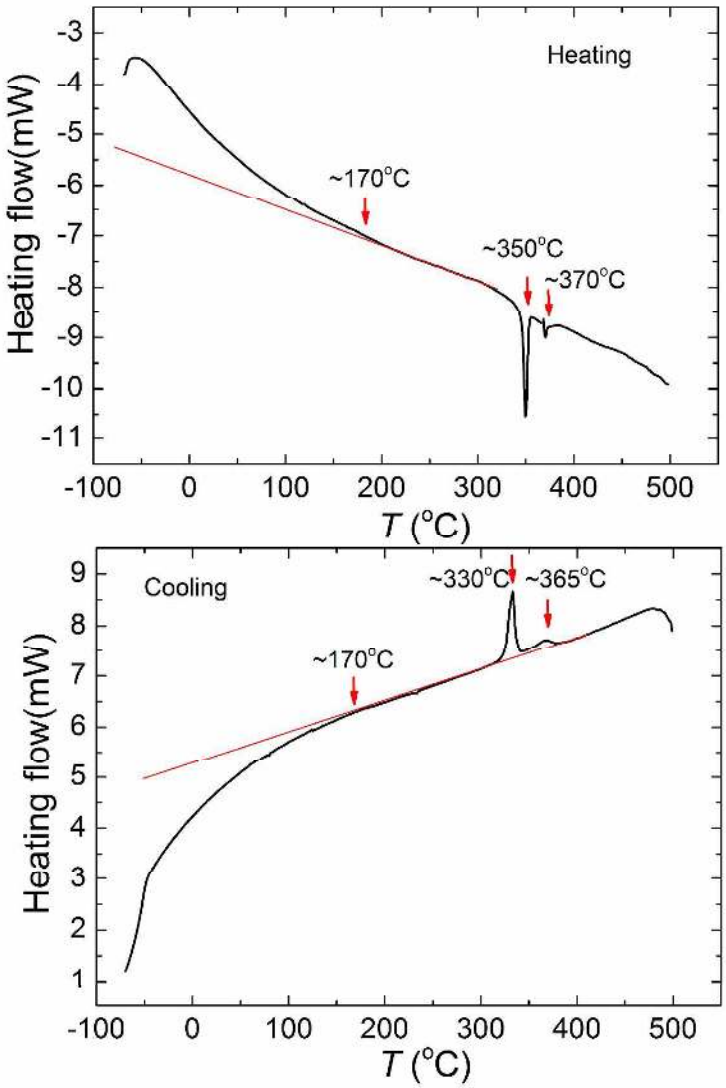

Fig. 6. DSC thermogram of $AgNbO_3$ powder on heating and cooling.

View Article Online
DOI: 10.1039/C6TA06353E

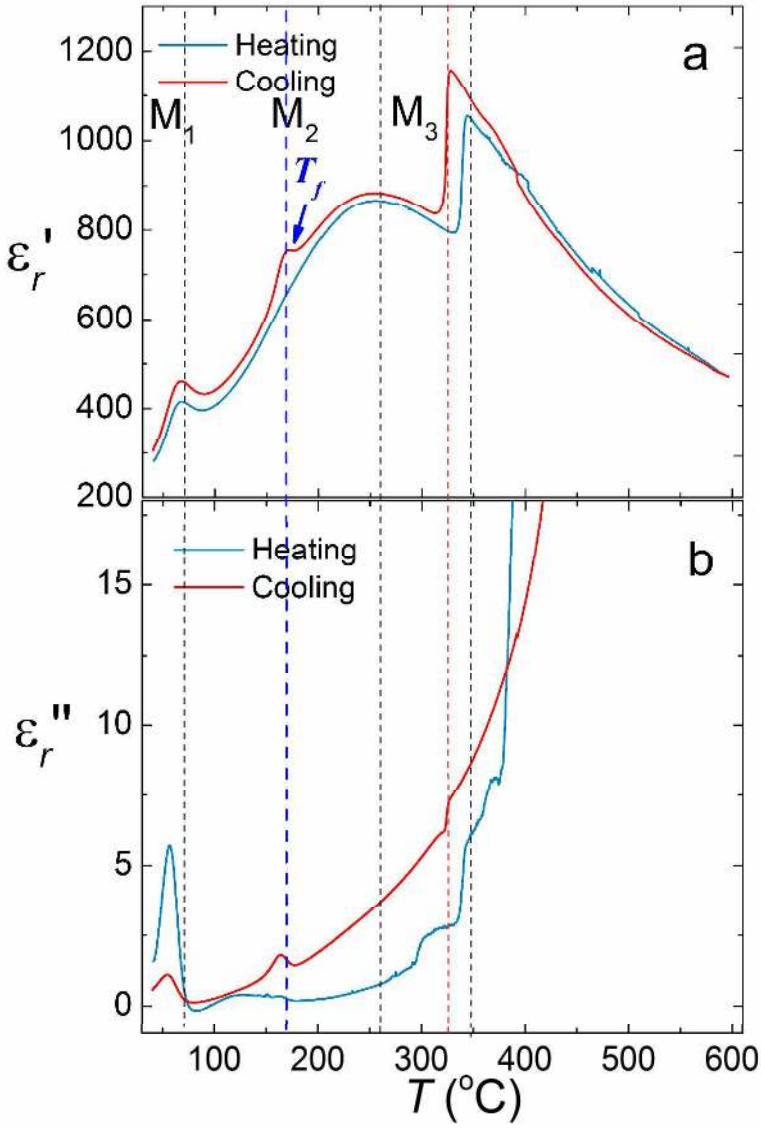

Fig. 7. Temperature dependence of (a) real (ε_r') and (b) imaginary (ε_r'') parts of dielectric permittivity in $AgNbO_3$.

View Article Online
DOI: 10.1039/C6TA06353E

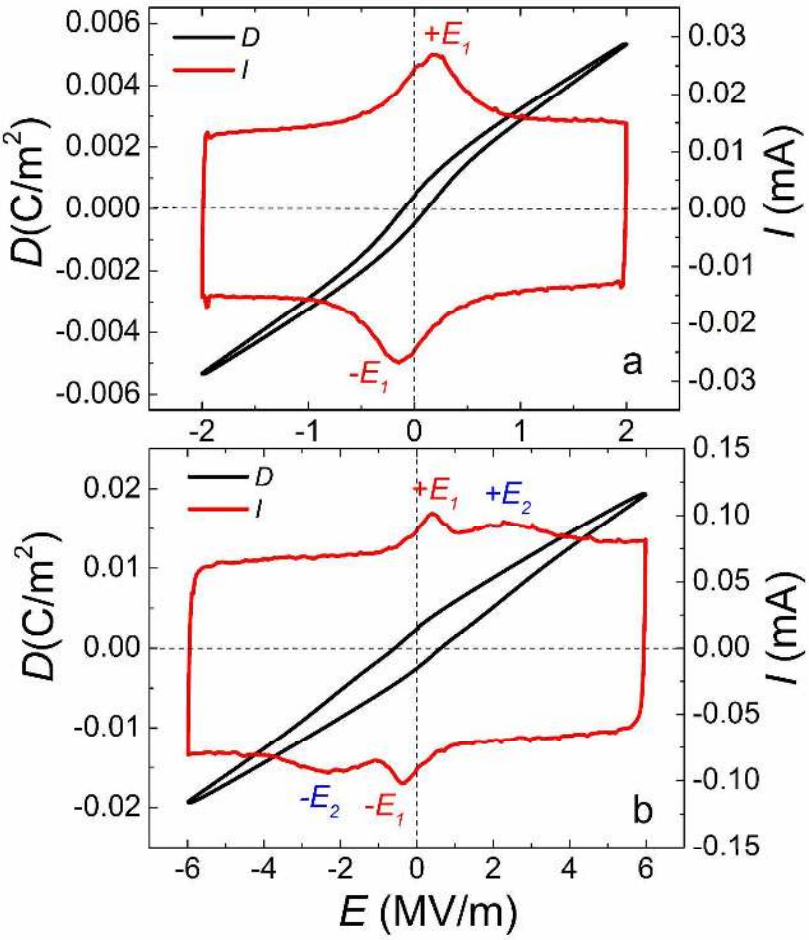

Fig. 8. Ferroelectric D-E and I-E loops measured at 10 Hz for $AgNbO_3$ ceramic at room temperature.

View Article Online
DOI: 10.1039/C6TA06353E

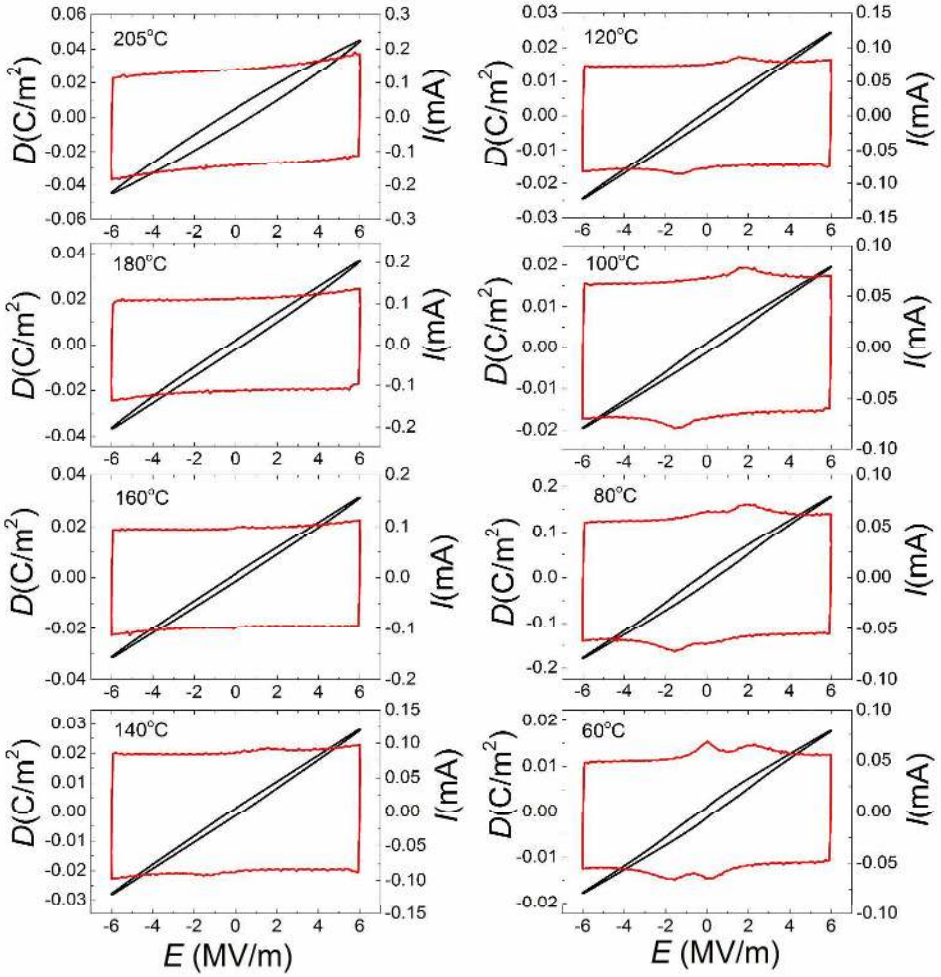

Fig. 9. Ferroelectric D-E and I-E loops measured at 10 Hz for $AgNbO_3$ ceramic at selected temperatures.

View Article Online
DOI: 10.1039/C6TA06353E

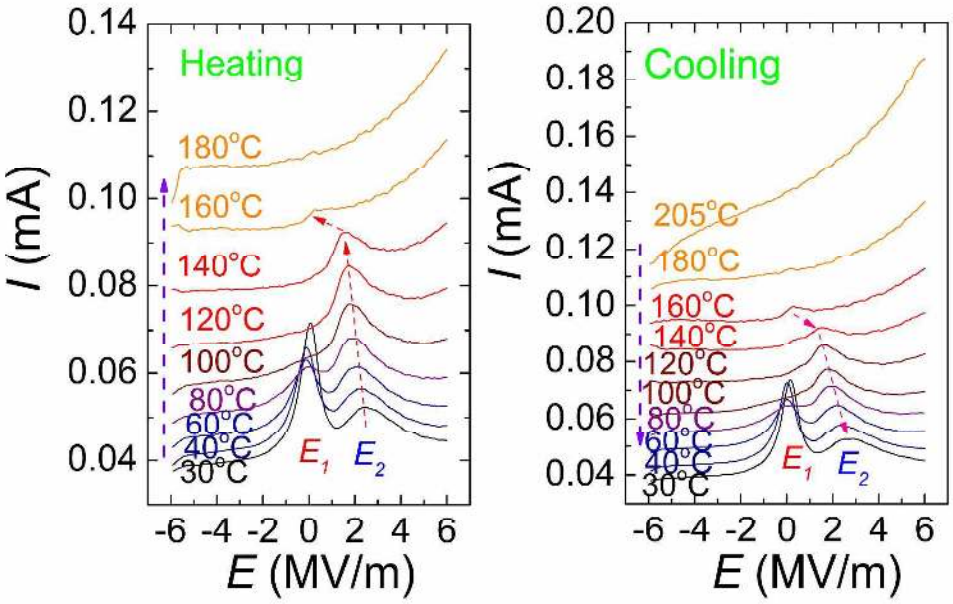

Fig. 10. Thermal dependence of current peaks during ferroelectric tests on $AgNbO_3$ ceramic.

View Article Online
DOI: 10.1039/C6TA06353E

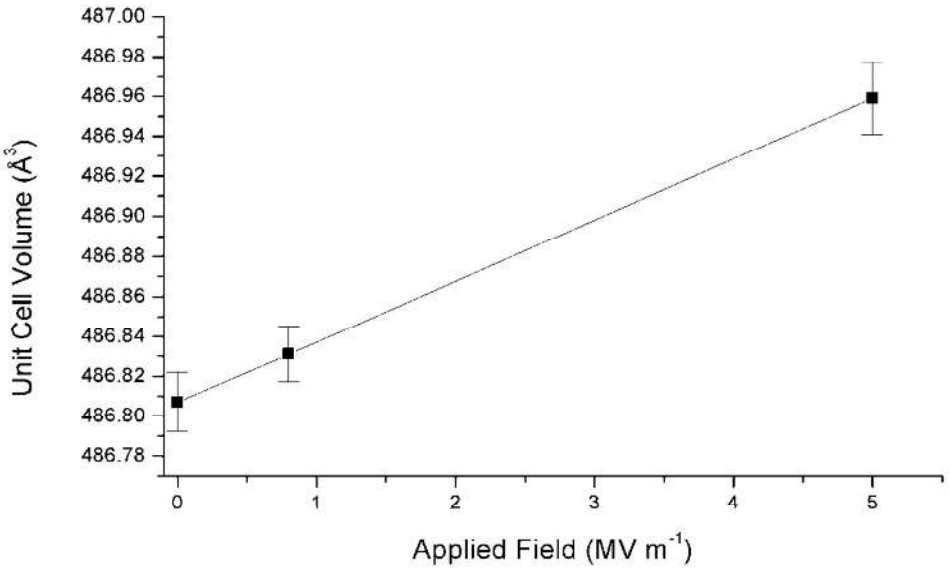

Fig. 11. Refined unit cell volume for $AgNbO_3$ ceramic after poling under different DC fields. Estimated standard deviations are indicated by error bars.

View Article Online
DOI: 10.1039/C6TA06353E

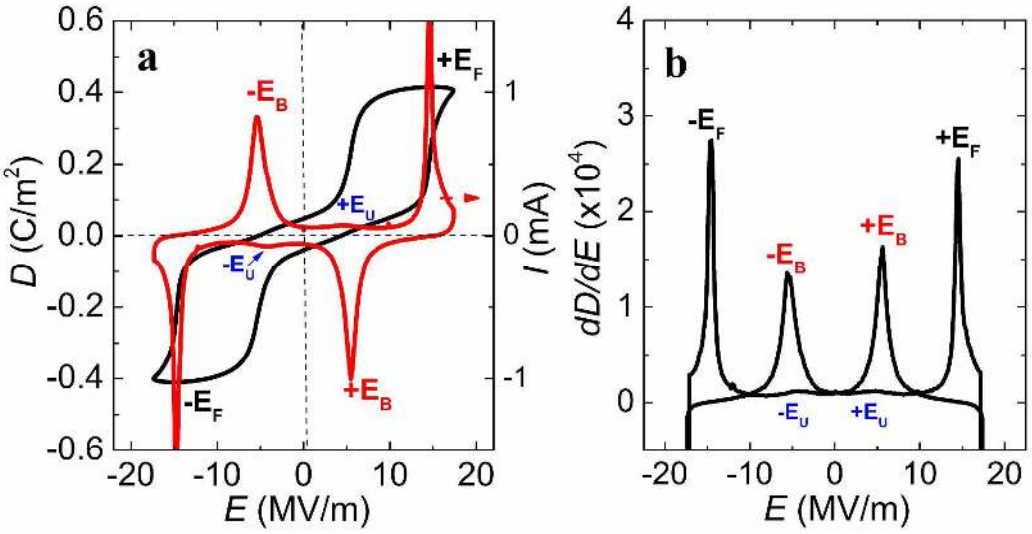

Fig. 12. High field Ferroelectric (a) D-E, I-E and (b) *dD/dE*-E loops measured at room temperature for $AgNbO_3$ ceramic at 1 Hz.

View Article Online
DOI: 10.1039/C6TA06353E

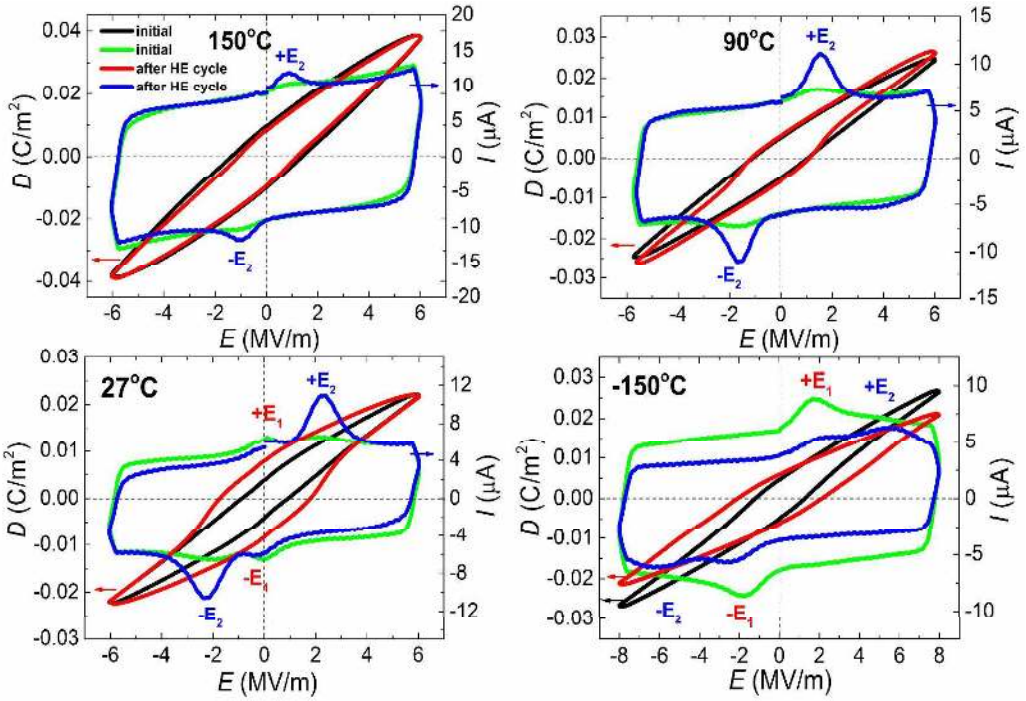

Fig. 13 A comparison of ferroelectric D-E and I-E loops measured at 0.5 Hz for a fresh sample (denoted as "initial") and the sample after high-field cycling(denoted as "after HE cycle").

View Article Online
DOI: 10.1039/C6TA06353E

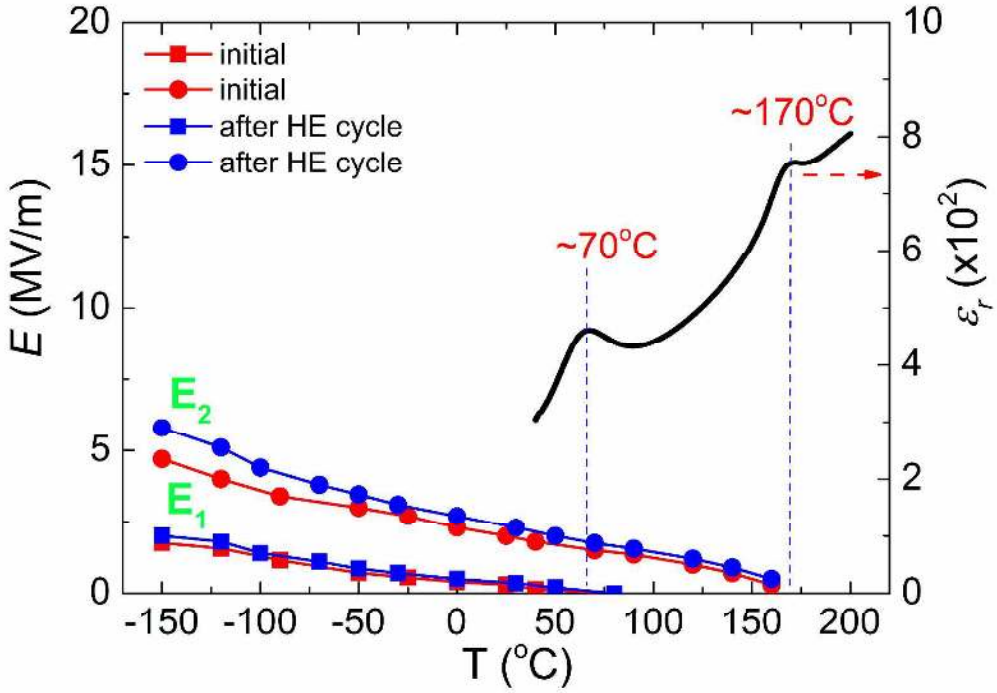

Fig. 14 Temperature dependence of domain switching fields E_1 and E_2 prior to and post high field cycling, compared to the temperature dependence of dielectric permittivity.